NUMERICAL SIMULATION OF THE FLOW OVER 2-D WINGMAST FOILS

Jhon Nero Vaz Goulart, jvaz@unb.br
Universidade de Brasília, Faculdade UnB Gama, Área Especial 2 Lote 14 Setor Central Gama-DF

Luciano Gonçalves Noleto, lucianonoleto@unb.br
Antonio C. P. Brasil Junior, brasiljr@unb.br
Universidade de Brasília, Faculdade de Tecnologia, Departamento de Engenharia Mecânica, Laboratório de Energia e Ambiente, 70910-900 - Asa Norte - Brasília, DF - Brasil

Abstract. *The present work employs XFOIL numerical code and a two-dimensional finite element method algorithm to study the flow around wingmast foils. The finite element code is a projection method-based algorithm for turbulent flow evaluation. The SST turbulence model is employed in the FEM code. In order to perform a complete evaluation, the following parameters are varied: Reynolds number and design shape. Design shape is based on mast/chord size. The effects on boundary layer are also investigated, by ranging mast/chord-size from 5% up to 50%. The angle of attack remains constant, 0 degrees. Flow simulations are carried out for Reynolds numbers from 250 000 up to 1000 000.*

Keywords: *Wingmast foils, Finite Element Method, Panel Method, Projection Methods.*

1. INTRODUCTION

Airfoil design and application is widely noticed in aerospace engineering. By using experimental facilities and numerical simulations several experiments were aimed to measure important features of these profiles. Main targets were always drag (C_d) and lift (C_l) coefficients, their variation and relationship with Reynolds number, surface conditions (roughness), free-stream turbulence and boundary layer transition (Somers and Maughmer (2003)).

Over past decades too much effort has been employed to develop families of airfoils for a suited purpose. Tailored airfoils had been used, mainly, for aircraft industry looking for an acceptable design in order to reach desirable characteristics under specific work conditions. In Harris (1990), a matrix of family supercritical airfoils was stressed. Coming into the light tailored airfoils coordinates with thickness and lift coefficients ranged from 2 to 18 percent of the chord and 0 to 1.0, respectively.

Despite vast aerospace engineering application, recently, attention has been focused on new subject. The search for renewable energy sources has enforced research to develop airfoils for wind turbines blades. According to Fuglsang *et al.* (2004), it has been very well reported that wind turbines airfoils should differ from traditional aviation airfoils. This fact has implied in a significant contribution to tailored airfoils for specific requirements. Papers from Timmer and van Rooji (2003) and Grasso (2010), are some examples of the most remarkable works on this subject. Other kind of tailored airfoils are the teardrop-shaped wingmasts. Teardrop wingmasts are formed by mast/sail combination and it can be designed based on any family of airfoil, only by setting the percentage of the chord that will be used.

This paper is aimed in order to rise awareness about teardrop wingmasts. Using NACA 0012 as baseline airfoil, wingmasts were designed and studied by numerical simulations. In order to evaluate those wingmasts, Reynolds number and design shape were varied. Design shape was based on mast/chord size. The effects on boundary layer are also investigated, by ranging mast/chord-size 5% , 30% and 50%, while angle of attack is kept as 0 degrees. Flow simulations are carried out for Reynolds numbers from 250000 up to 1000000.

2. DESIGN WINGMASTS FROM A PREVIOUS AIRFOIL

In this work wingmasts airfoils were based on modifying an existing airfoil. For this purpose a NACA 0012 airfoil was used, taking advantage from easy calculation to determine its shape. When mast and sail are put together the following characteristics should be taken into account: mast/chord-size and mast rotation. Mast/chord-size is the chord percentage covered by the mast. The mast ends where the sail starts, at mast/sail junction. With mast/chord-size chosen, mast rotation is determined. Mast rotation is the angle formed between leading edge and the mast/sail junction point. Figure 1 shows a NACA 0012 with mast/chord-size of 50% and mast rotation of 10 degrees.

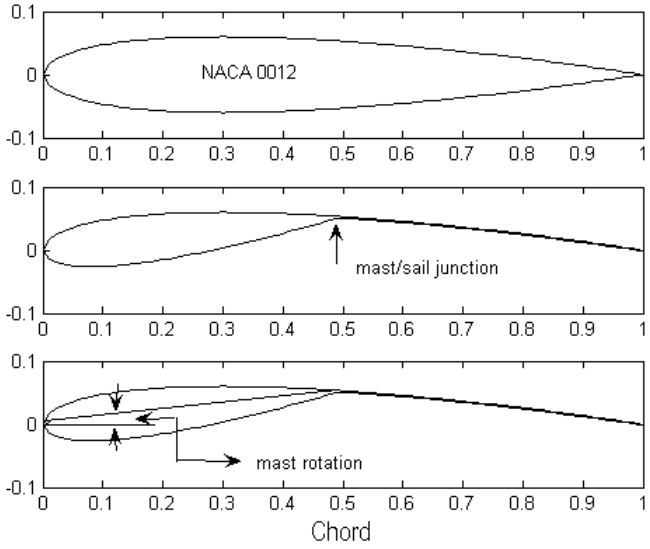

Figure 1. Main characteristics in wingmasts.

The easiest way to determine coordinates for the wingmast profile is given as follows (Figure 2):

- Select an existing airfoil;
- Chose mast/chord-size;
- Draw an auxiliary line linking leading edge to the mast/sail junction;
- Like a mirror, reflect upper surface of the mast around the drawn line. Remove the center line;

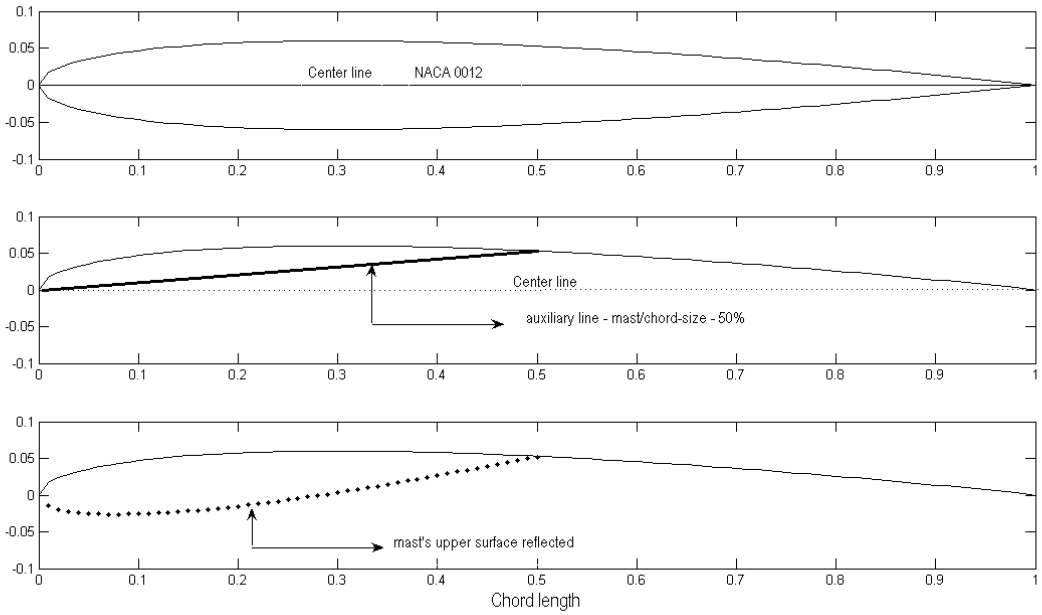

Figure 2. Steps for wingmasts construction.

Based upon what it just discussed above, Figure 3 presents the shape of wingmasts that will be analyzed during this work. Wingmasts mast/chord-size were ranged of 5%, 30% and 50%.

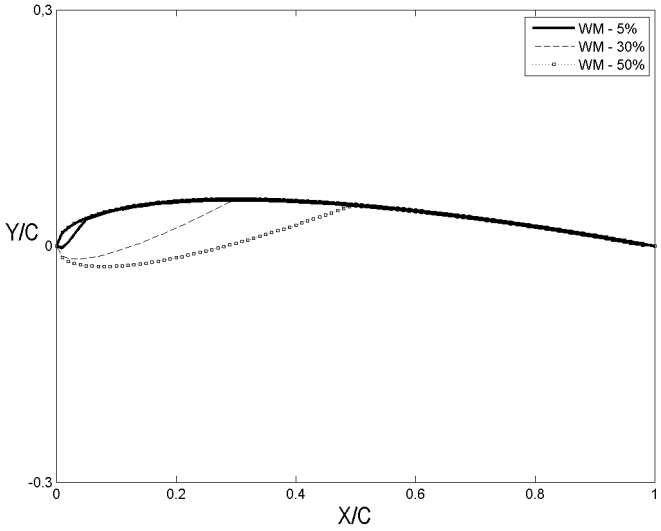

Figure 3. Wingmast design based on NACA 0012. Mast/chord from 5% up to 50%.

3. PROBLEM STATEMENT

The mass conservation and momentum equations for incompressible flows are written in a framework of turbulence modeling and defined in an open connected bounded domain $\Omega_t \times [0,T]$ in $\mathbb{R}^d$ (where d=2) with boundary $\Gamma_t = \partial\Omega_t$ such as:

$$\nabla.\mathbf{u} = \mathbf{0} \tag{1}$$

$$\frac{\partial \mathbf{u}}{\partial t} + \mathbf{u}\cdot\nabla\mathbf{u} = -\frac{1}{\rho}\nabla p + (\nu+\nu_T)\nabla^2\mathbf{u} + f \tag{2}$$

In those equations **u** and p are the mean velocity and pressure fields, ν and ν_T are the kinematic and turbulent viscosity, respectively, ρ is the fluid density and f is the source term. One can note that the problem is open, since the turbulent viscosity needs modeling. Modeling approach is given by the SST turbulence model (Menter *et al.* (2003)):

$$\frac{\partial k}{\partial t} + \mathbf{u}\cdot\nabla k = P_k - \beta' k\omega + \nabla\cdot\left[\left(\nu + \frac{\nu_t}{\sigma_k}\right)\right]\nabla k \tag{3}$$

$$\begin{aligned}\frac{\partial \omega}{\partial t} + \mathbf{u}\cdot\nabla\omega &= \alpha S^2 + \beta\omega + \nabla\cdot\left[\left(\nu + \frac{\nu_t}{\sigma_\omega}\right)\right]\nabla\omega \\ &+ 2(1-F_1)\sigma_{\omega 2} + \frac{1}{\omega}(\nabla k)(\nabla\omega)\end{aligned} \tag{4}$$

Here, k and ω are the turbulent kinetic energy and turbulent frequency respectively. Eddy viscosity is defined by:

$$\nu_t = \frac{\alpha_1 k}{\max(\alpha_1\omega, SF_2)} \tag{5}$$

S is an invariant measure of the rate-of-strain tensor and the blending functions F_1 and F_2 are given as follows:

$$F_1 = \tanh(\arg_1^4) \tag{6}$$

$$\arg_1 = \min\left[\max\left(\frac{\sqrt{k}}{\beta'\omega y}, \frac{500\nu}{y^2\omega}\right), \frac{4k}{CD_{k\omega}\sigma_{\omega 2}y^2}\right] \tag{7}$$

$$CD_{k\omega} = \max(2\frac{1}{\omega\sigma_{\omega 2}}\nabla k\nabla\omega, 1, 0\times 10^{-10}) \tag{8}$$

$$F_2 = \tanh(\arg_2^2) \tag{9}$$

$$\arg_2 = \max\left(\frac{2\sqrt{k}}{\beta'\omega y}, \frac{500\nu}{y^2\omega}\right) \tag{10}$$

Here, y is the distance to the nearest wall. A production limiter is used to avoid the excessive generation of turbulence in stagnation points (Menter *et al.* (2003)):

$$P_k = \mu_t S^2 \tag{11}$$

$$\widetilde{P_k} = \min(P_k, 10 \cdot \rho\beta^* k\omega) \tag{12}$$

The constants of the model are accounted as a linear combination of the corresponding constants of the $k-\varepsilon$ and $k-\omega$ models (Menter *et al.* (2003)):

$$\alpha = \alpha_1 F_1 + \alpha_2(1 - F_1) + ... \tag{13}$$

The constants are $\beta = 0.09$, $\alpha_1 = 5/9$, $\beta_1 = 3/40$, $\alpha_{k1} = 0.5$, $\sigma_{\omega 1} = 0.5$, $\alpha_2 = 0.44$, $\beta_2 = 0.0828$, $\sigma_{k2} = 1$, $\sigma_{\omega 2} = 0.856$. The ω-equation allows a near-wall formulation, which gradually switches from wall-functions to low-Reynolds near wall formulations (Menter *et al.* (2003)).

Boundary conditions are given by:

$$\mathbf{u}(x,t) = \mathbf{u}_d; \quad \text{on} \quad \Gamma_d \tag{14}$$

$$p(x,t) = p_{\text{ref}}; \quad \text{on} \quad \Gamma_o \tag{15}$$

$$k(x,t) = k_d; \quad \text{on} \quad \Gamma_d \tag{16}$$

$$\omega(x,t) = \omega_d; \quad \text{on} \quad \Gamma_d \tag{17}$$

For the above mentioned conditions, Γ_d represents the boundary where Dirichlet-type boundary conditions ($\mathbf{u}_d$, k_d, ω_d) are prescribed. Γ_o denotes the boundary where a reference pressure p_{ref} is prescribed.

4. Numerical Methodology

4.1 Time Discretization

The following methodology is designed to solve the equation system (1)-(4) by a semi-explicit iterative strategy, after time and spatial discretization. A framework of projection methods, given by Donea and Huerta (2003) is employed. One can define a time step $\Delta t > 0$ where a set of variables denoted by $(\mathbf{u}^n, p^n, k^n, \omega^n)$ is defined. The set of variables $(\mathbf{u}^{n+1}, p^{n+1}, k^{n+1}, \omega^{n+1})$ at the time $t + \Delta t$, is obtained by velocity and pressure splitting and calculation of turbulent quantities:

$$\frac{1}{\Delta t}(\mathbf{u}^* - \mathbf{u}^n) + \mathbf{u}^n \cdot \nabla\mathbf{u}^n = -\frac{1}{\rho}\nabla p^n + (\nu + \nu_T)\nabla^2\mathbf{u}^n + f \tag{18}$$

$$\frac{1}{\Delta t}\left(\mathbf{u}^{n+1} - \mathbf{u}^*\right) = -\frac{1}{\rho}\nabla(p^{n+1} - p^n) \tag{19}$$

$$\nabla.\mathbf{u}^{n+1} = 0 \tag{20}$$

$$\frac{1}{\Delta t}(k^* - k^n) + \mathbf{u}^n \cdot \nabla k^n = \left(\nu + \frac{\nu_t}{\sigma_k}\right)\nabla^2 k^n + f_k \tag{21}$$

$$\frac{1}{\Delta t}(\omega^* - \omega^n) + \mathbf{u}^n \cdot \nabla\omega^n = \left(\nu + \frac{\nu_t}{\sigma_\omega}\right)(\nabla^2\omega^n) + f_\omega \tag{22}$$

Where:

$$f_k = P_k - \beta' k\omega \tag{23}$$

$$f_\omega = \alpha S^2 + \beta\omega^n + 2(1 - F_1)\sigma_{\omega^n 2} + \frac{1}{\omega^n}(\nabla k)(\nabla\omega^n) \tag{24}$$

This algorithm introduces predicted quantities $\mathbf{u}^*$, k^* and ω^*. From those, only $\mathbf{u}^*$ will be corrected at each step. This algorithm transforms one problem into a sum of two problems: One made by a pure advection and other made by pure

diffusion. Both are solved sequentially at each step of the time integration (Donea and Huerta (2003)). When one takes the divergent of equation 19 and uses on equation 20, pressure equation assumes the form of a Poisson problem:

$$\nabla^2 \left(p^{n+1} - p^n\right) = \frac{\rho}{\Delta t} \nabla . \mathbf{u}^* \tag{25}$$

The boundary condition for this equation is given as follows:

$$\nabla \left(p^{n+1} - p^n\right) . \mathbf{n} = \frac{\rho}{\Delta t} \mathbf{u}^* . \mathbf{n} \text{ on } \Gamma_o \tag{26}$$

Remark:
This algorithm is called Incremental Projection Scheme (Guermond and Quartapelle (2000)). It is based on a pressure correction methodology. These schemes are time-marching techniques composed of substeps at each time step. Pressure can be treated explicitly or ignored at the first substep. Its solution will be used to project the velocity into a divergent-free field. This work uses the following implementation: The pressure is maintained at the first substep, corrected at the next substep and used to correct the velocity at the final substep. This implementation improves convergence properties, as reported at the literature (Codina (2001)).

4.2 Standard Weak Form

Some definitions must be presented to show the standard weak form (Codina and Blasco (2000)). One can denote $L^2(\Omega_t)$ as the space of squared integrable functions over the domain Ω_t and $H^1(\Omega_t)$ as the Sobolev space where its derivatives are also squared integrable. The internal product of $L^2(\Omega_t)$ is denoted by $(.,.) = \int_{\Omega_t} .. \, d\Omega_t$ and $H_0^1(\Omega_t)$ is the sub-space of functions with zero value on boundaries.

One can write weight functions $\mathbf{v} \in V = H_0^1(\Omega_t)$ and $q \in Q = L^2(\Omega_t)/\mathbb{R}$, and consider $\mathbf{u} \in U = H^1(\Omega_t)$. The weak form of equations 18, 19, 21, 22 and 25 can be written as follows:

$$m_u(\Delta \mathbf{u}^*, \mathbf{v}) + c_u(\mathbf{u}^n, \mathbf{u}^n, \mathbf{v}) + (\nu + \nu_T)\, a_u(\mathbf{u}^n, \mathbf{v}) + \frac{1}{\rho} b(p, \mathbf{v}) = (f, \mathbf{v}) \tag{27}$$

$$a(\Delta p, q) = -\frac{\rho}{\Delta t}\, b(\mathbf{u}^*, q) \tag{28}$$

$$m(\Delta \mathbf{u}^{n+1}, \mathbf{v}) = -\frac{1}{\rho}\, b(\Delta p, \mathbf{v}) \tag{29}$$

$$m_k(\Delta k^*, \mathbf{v}) + c_k(k^n, \mathbf{u}^n, \mathbf{v}) + \, D_k a_k(k^n, \mathbf{v}) = (f_k, \mathbf{v}) \tag{30}$$

$$m_\omega(\Delta \omega^*, \mathbf{v}) + c_\omega(\omega^n, \mathbf{u}^n, \mathbf{v}) + \, D_\omega a_\omega(\omega^n, \mathbf{v}) = (f_\omega, \mathbf{v}) \tag{31}$$

Where:

$$D_k = \left(\nu + \frac{\nu_T}{\sigma_k}\right) \tag{32}$$

$$D_\omega = \left(\nu + \frac{\nu_T}{\sigma_\omega}\right) \tag{33}$$

Where the following forms are introduced:

$$m_u(\mathbf{u}, \mathbf{v}) := \frac{1}{\Delta t}(\mathbf{u}, \mathbf{v}) \; ; \; c_u(\mathbf{u}, \mathbf{u}, \mathbf{v}) := (\mathbf{u} \cdot \nabla \mathbf{u}, \mathbf{v}) \tag{34}$$

$$a(\mathbf{u}, \mathbf{v}) := (\nabla \mathbf{u}, \nabla \mathbf{v}) \; ; \; b(q, \mathbf{v}) := (q, \nabla . \mathbf{v}) \tag{35}$$

$$m_k(k, \mathbf{v}) := \frac{1}{\Delta t}(k, \mathbf{v}) \; ; \; c_k(k, \mathbf{u}, \mathbf{v}) := (\mathbf{u} \cdot \nabla k, \mathbf{v}) \tag{36}$$

$$m_\omega(\omega, \mathbf{v}) := \frac{1}{\Delta t}(\omega, \mathbf{v}) \; ; \; c_\omega(\omega, \mathbf{u}, \mathbf{v}) := (\mathbf{u} \cdot \nabla \omega, \mathbf{v}) \tag{37}$$

The increments of all fields are given by:

$$\begin{aligned}
\Delta\mathbf{u}^* &= \mathbf{u}^* - \mathbf{u}^n \\
\Delta\mathbf{u}^{n+1} &= \mathbf{u}^{n+1} - \mathbf{u}^* \\
\Delta p &= p^{n+1} - p^n \\
\Delta k^* &= k^* - k^n \\
\Delta\omega^* &= \omega^* - \omega^n
\end{aligned} \tag{38}$$

Remark:
The method described here is based on a first-order time discretization. Superior order discretizations can be used accordingly with the problem and with desired precision and computational cost. Therefore, the solution of equations 27 to 31 will lead to a consistent formulation of all calculated fields at time $t + \Delta t$.

4.3 Spatial Discretization

Let $T^h(\Omega_t)$ a regular partition of the domain Ω_t where the finite element spaces $Q_h \subset Q$, $V_h \subset V$ and $U_h \subset U$ are constructed. The discrete problem equivalent to the weak form can be written as: Given $u_h^n, p_h^n, k_h^n, \omega_h^n$, find $u_h^{n+1}, p_h^{n+1}, k_h^{n+1}, \omega_h^{n+1} \in U_h \times Q_h$, such as $\forall\ \{\mathbf{v_h}, q_h\} \in V_h \times Q_h$:

$$\begin{aligned}
m_u(\Delta\mathbf{u}_h^*, \mathbf{v}_h) &= -c_u(\mathbf{u}_h^n, \mathbf{u}_h^n, \mathbf{v}_h) - \nu\, a_u(\mathbf{u}_h^n, \mathbf{v}_h) - \\
&- \frac{1}{\rho} b(p_h, \mathbf{v}_h) - \mathbf{s}_u(\mathbf{u}_h^n, \mathbf{u}_h^n, \mathbf{v}_h) + (f, \mathbf{v}_h)
\end{aligned} \tag{39}$$

$$a(\Delta p_h, q_h) = -\frac{\rho}{\Delta t}\, b(\mathbf{u}_h^*, q_h) \tag{40}$$

$$m(\mathbf{u}_h^{n+1}, \mathbf{v}_h) = -\frac{1}{\rho}\, b(\Delta p_h, \mathbf{v}_h) \tag{41}$$

$$m_k(\Delta k_h^*, \mathbf{v}_h) + c_k(k_h^n, \mathbf{u}_h^n, \mathbf{v}_h) + \ D_k a_k(u_h^n, \mathbf{v}_h) = (f_k, \mathbf{v}_h) \tag{42}$$

$$m_\omega(\Delta\omega_h^*, \mathbf{v}_h) + c_\omega(\omega_h^n, \mathbf{u}_h^n, \mathbf{v}_h) + \ D_\omega a_\omega(\omega_h^n, \mathbf{v}_h) = (f_\omega, \mathbf{v}_h) \tag{43}$$

The discrete form is obtained similarly as the methods described in Codina and Folch (2004). The extra term at equation 39($\mathbf{s}_u(\mathbf{u}_h^n, \mathbf{u}_h^n, \mathbf{v}_h)$) is responsible to ensure stability in convective-dominated regimes. It is written as:

$$\mathbf{s}_u(\mathbf{u}_h^n, \mathbf{u}_h^n, \mathbf{v}_h) = (\mathbf{u}_h^n \cdot \nabla\mathbf{u}_h^n, \Delta t(\mathbf{u}_h^n \cdot \nabla\mathbf{v})) \tag{44}$$

Considering the dimension of the spaces given by $dim(V_h) = dim(U_h) = dim(Q_h) = N$ and base functions denoted by $\{\mathbf{N}_i; i = 1, N\}$ and $\{\mathbf{N}_j; j = 1, N\}$, the discrete problem matrix form is given as follows:

Step 1: Velocity Calculation:

$$\mathbf{M_u}.\mathbf{\Delta u}_h^* = \mathbf{F}_u^*(\mathbf{u}_h^n, \mathbf{v}_h^n, p_h^n) \tag{45}$$

Step 2: Pressure Calculation:

$$\mathbf{A}.\Delta p_h = \mathbf{F}_p(\mathbf{u}_h^*) \tag{46}$$

Step 3: Velocity projection in a divergent-free space:

$$\mathbf{M_u}.\mathbf{\Delta u}_h^{n+1} = \mathbf{F}_u(\Delta p_h) \tag{47}$$

Step 4: Kinetic turbulent energy calculation:

$$\mathbf{M}_k.\Delta k_h^* = \mathbf{F}_k^*(k_h^n, \mathbf{v}_h^n) \tag{48}$$

Step 5: Turbulent frequency calculation:

$$\mathbf{M}_\omega.\Delta\omega_h^* = \mathbf{F}_\omega^*(\omega_h^n, \mathbf{v}_h^n) \tag{49}$$

Where the matrices $\mathbf{M_u}, \mathbf{M}_k$ and $\mathbf{M}_\omega$ are the mass matrices for the velocity and turbulent quantities respectively and $\mathbf{A}$ is the Laplacian matrix for the pressure. Those matrices are given as follows:

$$\mathbf{M}_{ij} = \frac{1}{\Delta t}(\mathbf{N}_i, \mathbf{N}_j) \;\; ; \;\; \mathbf{A}_{i,j} = (\nabla \mathbf{N}_i, \nabla \mathbf{N}_j) \tag{50}$$

The vectors $\mathbf{F}_u^*$, $\mathbf{F}_p$ and $\mathbf{F}_u$ are related to the right hand side discretization of the matrix equations on steps 1 to 3. The boundary integral terms, related to the boundary conditions, are added into these vectors.

Remarks:

- The linear system solution of steps 1 and 3 involve the mass matrix. In order to enhance the convergence rate, this matrix is lumped in a diagonal form. The lumping is performed once in the beginning of the iterative process.
- The linear system for the pressure correction problem, step 2, is solved by the Conjugated Gradient Method, preconditioned by partial Cholesky factorization. This matrix is stored by a Morse strategy, and the preconditioning is also performed once when this matrix is firstly computed.
- The time step is controlled by a weighted average between convective (Δt_{cov}) and diffusive (Δt_{diff}) time steps, given as follows (Zienkiewicz *et al.* (2005)):

$$\Delta t \leqslant \frac{\Delta t_{cov} \Delta t_{diff}}{\Delta t_{covdv} + \Delta t_{diff}} \tag{51}$$

5. RESULTS

The FEM-simulated domain and its mesh are displayed at figure 4:

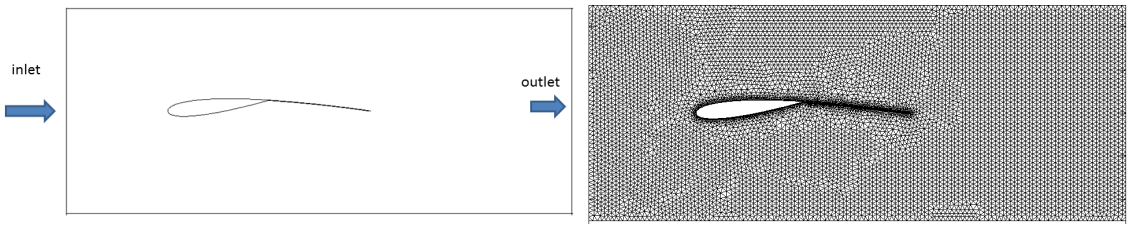

Figure 4. Domain Display and Calculation Mesh

At the inlet, the velocity is set to give the chord-based Reynolds numbers mentioned before (250000, 500000 and 1000000). A zero reference pressure is imposed at the outlet boundary condition. At the wingmast, a no-slip condition is imposed. The mesh has 9321 nodes e 17536 P1 elements. The lift and drag coefficients are given as follows:

$$C_l = \frac{F_l}{0.5\rho U_0^2 A} \tag{52}$$

$$C_d = \frac{F_d}{0.5\rho U_0^2 A} \tag{53}$$

Before starting any analysis it is important to take into account XFOIL code's limitations. Theoretical method employed in XFOIL is strictly two-dimensional. Therefore, lift and drag coefficients from XFOIL may disagree with experimental or numerical results based on Navier-Stokes code. However, it might be a good starting point. It is important to remind the lack of experimental data at the literature does not allow validation of numerical results presented here. In the future, experimental results may show disagreement with the numerical ones obtained by the FEM Navier-Stokes code.

The obtained results showed that Reynolds number increase do not affect flow topology. A low pressure zone appears in the mast/chord-size 5% wingmast, which corresponds to a recirculation cell at the vorticity contours on the windward side at mast/sail junction (Figures 6(a) and 7(a)). This recirculation zone gives the wingmast a more bluff format, as displayed at figure 5(a). One can also note higher pressure zones on the windward side at the mast/sail junction for wingmasts foils 30 (Figures 6(b) and 7(b)) and 50% (Figures 6(c) and 7(c)).

Dashed line at figure 5 display the boundary layer prediction by XFOIL. One can note similarities between those visualizations and the vorticity contours displayed at figure 7. These similarities give a hint on the boundary layer behavior above and below the wingmast. One can note flow separation at the moment that flow impinges on the leading edge, creating the recirculation zone on the 5% mast type.

Table 1 shows values of C_l and C_d for both simulations. When one observes the lift coefficient, only 5% mast/chord wingmast present higher values. However, their drag coefficients have almost been increased by a factor of two, yielding lower values of the ratio C_l/C_d. These results can be linked to the recirculation zone observed at the visualizations. One can state that the recirculation zone contributes on lift increase at the cost of the drag increase.

Similar patterns are noticed at the FEM simulation. The lift results are close to XFOIL lift data, while the drag results are apart from the XFOIL data. As a consequence, the lift-drag ratio of the FEM code is also apart. This difference is explained by the algorithm formulation. XFOIL employs a potential formulation, while the FEM code gives an approximate solution of the Navier-Stokes equations. For better drag results, one must generate the mesh to better capture viscous effects at the wingmast, alongside experimental results.

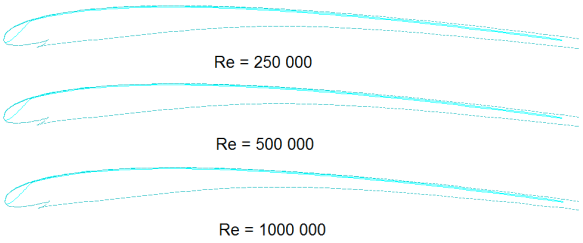

(a) Mast/chord - size:5%

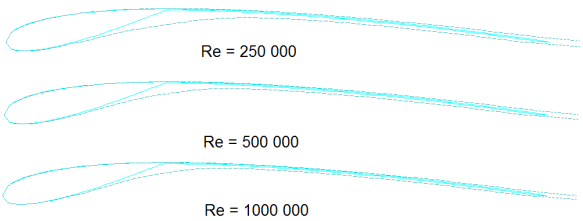

(b) Mast/chord - size:30%

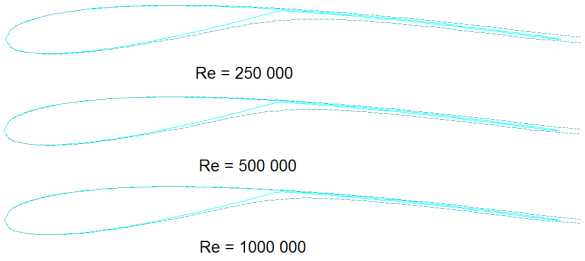

(c) Mast/chord - size:50%

Figure 5. Flow around wingmast - Calculated with XFOIL

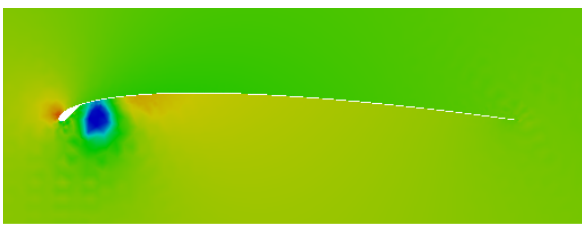

(a) Mast/chord - size:5%

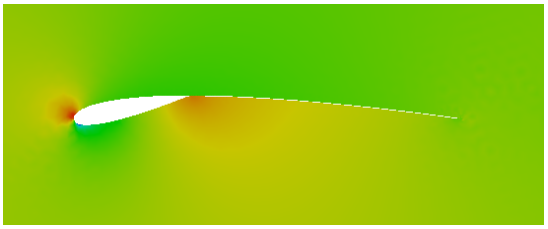

(b) Mast/chord - size:30%

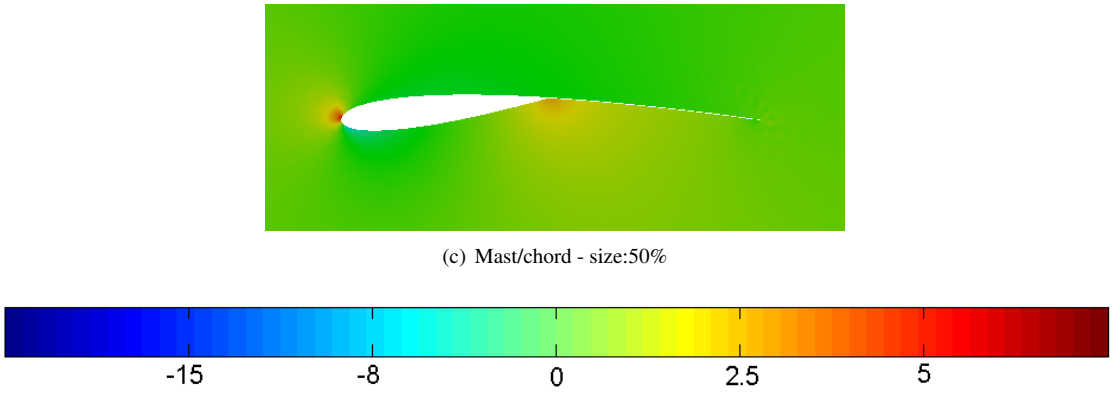

(c) Mast/chord - size:50%

Figure 6. Pressure visualizations - Calculated with FEM code

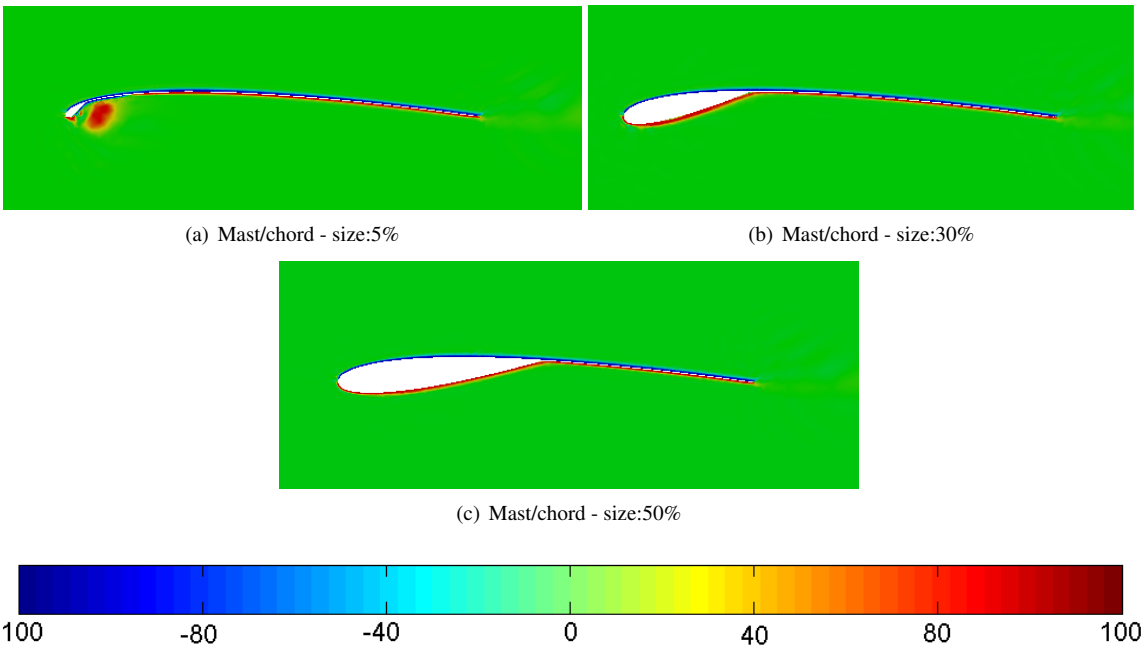

(a) Mast/chord - size:5%

(b) Mast/chord - size:30%

(c) Mast/chord - size:50%

Figure 7. Vorticity visualizations - Calculated with FEM code

Table 1. Lift Coefficients

	XFOIL	FEM	XFOIL	FEM	XFOIL	FEM
Reynolds (x 1000)	250	250	500	500	1000	1000
M/C - 5%	0.518	0.6752	0.522	0.5062	0.526	0.409
M/C - 30%	0.471	0.598	0.475	0.4437	0.478	0.5102
M/C - 50%	0.422	0.5922	0.426	0.4776	0.429	0.3575

Table 2. Drag Coefficients

	XFOIL	FEM	XFOIL	FEM	XFOIL	FEM
Reynolds (x 1000)	250	250	500	500	1000	1000
M/C - 5%	0.027	0.0128	0.025	0.0078	0.024	0.0059
M/C - 30%	0.016	0.01614	0.013	0.0105	0.012	0.01147
M/C - 50%	0.024	0.00143	0.011	0.00875	0.011	0.00611

Table 3. Lift-Drag Ratio

	XFOIL	FEM	XFOIL	FEM	XFOIL	FEM
Reynolds (x 1000)	250	250	500	500	1000	1000
M/C - 5%	19.241	52.75	20.710	64.89	22.000	69,32
M/C - 30%	30.055	37.05	37.205	42.25	43.633	44,48
M/C - 50%	28.903	41,41	34.521	54,58	40.256	58,51

6. CONCLUSIONS

Numerical simulations of wingmast-type airfoils were performed by a FEM code and XFOIL. Results were shown by boundary layer prediction obtained by XFOIL, and pressure and vorticity visualizations obtained by the FEM code. Lift, drag and the lift-drag ratio were calculated and compared for both simulations.

Low pressure zones were observed at the visualizations. An increase of Reynolds number also seems do not affect pressure distribution for the same wingmast. One can note similarities between boundary layer predictions and vorticity contours. It was also noted a relationship between the recirculation zone and the lift decrease when the mast-chord percentage increases. The recirculation zone increases the lift, at the cost of the drag increase. Comparison between FEM and XFOIL results showed similarities at the lift, but differences at the drag and lift-drag ratio. However, the increasing pattern of the ratio is observed by both simulations.

One can conclude that the results are coherent with each other, but further analysis is needed for full characterization of wingmast flow. In the future, experimental studies must be conducted to validate the relation between the lift and recirculation zones below the mast.

7. REFERENCES

Codina, R., 2001. "Pressure stability in fractional step finite element methods for incompressible flows". *Journal of Computational Physics*, Vol. 170, No. 112-140.

Codina, R. and Blasco, J., 2000. "Stabilized finite element method for the transient navier-stokes equations based on a pressure gradient projection". *Computer Methods in Applied Mechanics and Engineering*, Vol. 182, No. 3-4, pp. 277–300.

Codina, R. and Folch, A., 2004. "A stabilized finite element predictor-corrector scheme for the incompressible navier-stokes equations using a nodal-based implementation". *International Journal for Numerical Methods in Fluids*, Vol. 44, No. 5, pp. 483–503.

Donea, J. and Huerta, A., 2003. *Finite Element Method for Flow Problems*. Wiley.

Fuglsang, P., Bak, C., Gaunaa, M. and Antoniou, I., 2004. "Design and verification of the ris -b1 airfoil family for wind turbines". *Journal of Solar Energy Engineering*, Vol. 126, pp. 1002–1010.

Grasso, F., 2010. "Usage of numerical optimization in wind turbine airfoil design". *AIAA-2010-4404*.

Guermond, J. and Quartapelle, L., 2000. "A projection fem for variable density incompressible flows". *Journal of Computational Physics*, Vol. 165, No. 1, pp. 167–188.

Harris, C.D., 1990. "A matrix of family-related airfoils". *NASA TP-2969*.

Menter, F.R., Kuntz, M. and Langtry, R., 2003. "Ten years of industrial experience with the sst turbulence model". *Turbulence, Heat and Mass Transfer*, Vol. 4.

Somers, D.M. and Maughmer, M.D., 2003. "Theoretical aerodynamic analyses of six airfoils for use on small wind turbines". Technical report.

Timmer, W.A. and van Rooji, A., 2003. "Summary of the delft university wind turbine dedicated airfoils". *AIAA-2003-0352*.

Zienkiewicz, O.C., Taylor, R.L. and Nithiarasu, P., 2005. *The Finite Element Method for Fluid Dynamics*. Elsevier, 6th edition.

8. Responsibility notice

The author(s) is (are) the only responsible for the printed material included in this paper